LAWRENCE
LIVERMORE
NATIONAL
LABORATORY

LLNL-JRNL-472291

Radiation-Hydrodynamic Simulations of Massive Star Formation with Protostellar Outflows

A. J. Cunningham, R. I. Klein, M. R. Krumholz, C. F. McKee

March 7, 2011

Astrophysical Journal

Disclaimer

This document was prepared as an account of work sponsored by an agency of the United States government. Neither the United States government nor Lawrence Livermore National Security, LLC, nor any of their employees makes any warranty, expressed or implied, or assumes any legal liability or responsibility for the accuracy, completeness, or usefulness of any information, apparatus, product, or process disclosed, or represents that its use would not infringe privately owned rights. Reference herein to any specific commercial product, process, or service by trade name, trademark, manufacturer, or otherwise does not necessarily constitute or imply its endorsement, recommendation, or favoring by the United States government or Lawrence Livermore National Security, LLC. The views and opinions of authors expressed herein do not necessarily state or reflect those of the United States government or Lawrence Livermore National Security, LLC, and shall not be used for advertising or product endorsement purposes.

Radiation-Hydrodynamic Simulations of Massive Star Formation with Protostellar Outflows

Andrew J. Cunningham[1], Richard I. Klein[1,2], Mark R. Krumholz[3], Christopher F. McKee[2,4]

ajcunn@gmail.com

ABSTRACT

We report the results of a series of AMR radiation-hydrodynamic simulations of the collapse of massive star forming clouds using the ORION code. These simulations are the first to include the feedback effects protostellar outflows, as well as protostellar radiative heating and radiation pressure exerted on the infalling, dusty gas. We find that that outflows evacuate polar cavities of reduced optical depth through the ambient core. These enhance the radiative flux in the poleward direction so that it is 1.7 to 15 times larger than that in the midplane. As a result the radiative heating and outward radiation force exerted on the protostellar disk and infalling cloud gas in the equatorial direction are greatly diminished. The simultaneously reduces the Eddington radiation pressure barrier to high-mass star formation and increases the minimum threshold surface density for radiative heating to suppress fragmentation compared to models that do not include outflows. The strength of both these effects depends on the initial core surface density. Lower surface density cores have longer free-fall times and thus massive stars formed within them undergo more Kelvin contraction as the core collapses, leading to more powerful outflows. Furthermore, in lower surface density clouds the ratio of the time required for the outflow to break out of the core to the core free-fall time is smaller, so that these clouds are consequently influenced by outflows at earlier stages of collapse. As a result, outflow effects are strongest in low surface density cores and weakest in high surface density one. We also find that radiation focusing in the direction of outflow cavities is sufficient to prevent the formation of radiation pressure-supported circumstellar gas bubbles, in contrast to models which neglect protostellar outflow feedback.

[1]Lawrence Livermore National Laboratory, Livermore, CA 94550

[2]Department of Astronomy, University of California Berkeley, Berkeley, CA 94720

[3]Department of Astronomy and Astrophysics, University of California Santa Cruz, Santa Cruz, CA 94560

[4]Department of Physics, University of California Berkeley, Berkeley, CA 94720

Subject headings: (stars:) binaries: general, stars: formation, stars: pre-main sequence, stars: winds, outflows

1. Introduction

Stars of all masses undergo energetic, bipolar mass loss during their formation (Shepherd 2003; Richer et al. 2000). These outflows feed energy back into large-scale turbulent motions that support clouds against collapse, may play a role in dispersing clouds entirely (Norman & Silk 1980; McKee 1989; Nakamura & Li 2007; Carroll et al. 2010; Arce et al. 2010) and regulate the final mass of the central star (Matzner & McKee 2000; Arce & Sargent 2006; Wang et al. 2010). Massive stars likely provide the dominant source of radiation feedback in the evolution of their parent molecular clouds and any subsequent star formation therein. Although much progress has been made both observationally and theoretically, a comprehensive picture of massive star formation and the role of feedback from massive stars in mediating the star formation process remains to be elucidated (Zinnecker & Yorke 2007).

Observational evidence supports a picture where accretion and outflow ejection processes at work in the formation of high-mass stars proceed as a "scaled-up" version of their low-mass, solar-type counterparts. Interferometric molecular line measurements have detected quiescent compact cores within dense, infrared dark clouds of mass $\sim 100 M_\odot$ (Swift 2009) as likely progenitors to the onset of high-mass star formation. Observational surveys have established a correlation between molecular outflow mass-loss and source luminosity (Shepherd & Churchwell 1996; Richer et al. 2000) and between circumstellar mass and luminosity from 0.1 to $10^5 L_\odot$ (Saraceno et al. 1996; Chandler & Richer 2000). Several authors have detected molecular outflows from massive protostars with collimation factors of 2 to 10 (Zhang et al. 2001; Beuther et al. 2002a,c, 2003, 2004; Qiu et al. 2007; López-Sepulcre et al. 2011), similar to that of low-mass stars (Bachiller 1996). Radio thermal continuum emission jets, commonly associated with low-mass protostars (Rodriguez 1997), have also been identified near protostellar sources as luminous as $\sim 10^5 L_\odot$ (Torrelles et al. 1997; Curiel et al. 2006). Detection of synchrotron emission arising from the jet in one massive young stellar object gives support to the notion of a common magnetic driving mechanism to protostellar outflow from stars of all masses (Carrasco-González et al. 2010). Because high-mass accretion disks are deeply embedded in dusty envelopes, they are particularly difficult to observe directly. A few such detections have, however, been made by maser emission sources (Hutawarakorn et al. 2002), in high-resolution submillimeter dust emission (Patel et al. 2005) and in near-infrared observations where winds from nearby sources have cleared dust from the line of sight (Nürnberger et al. 2007). These observations suggest that massive stars form through

disk accretion in direct analogy to the formation of low-mass stars.

Several key theoretical aspects distinguish high and low-mass star formation despite the broad similarity of the observed outflow and ejection phenomena. Massive stars are shorter-lived and produce more sources of energetic feedback into their environment than their low-mass counterparts. O stars radiate their gravitational binding energy and reach the main sequence on Kelvin-Helmholtz timescales of $\lesssim 10^4$ yr whereas solar type stars require $\gtrsim 10^7$ yr. Stars with masses $\gtrsim 10\mathrm{M}_\odot$ therefore begin nuclear burning while they are still embedded within and accreting from the circumstellar envelope (Shu et al. 1987). The resultant spherically-averaged radiation pressure on dust grains in the infalling gas exceeds the gravitational pull from the central star (Larson & Starrfield 1971). Massive stars can therefore only form by accretion if some mechanism is in place to focus the outward radiative flux away from the infalling envelope. A variety of focusing mechanism have been suggested (Nakano 1989; Jijina & Adams 1996; Yorke & Sonnhalter 2002; Krumholz et al. 2009; McKee & Ostriker 2007; Kuiper et al. 2010), including the one of central interest for this paper, beaming of radiation in the cavities produced by protostellar outflows. (Krumholz et al. 2005). Once the embedded stars reach the main sequence, ionizing photons generate HII regions, strongly affecting the physical structure and chemistry of their environment. Recent observation suggests the existence of stars as massive as $300\mathrm{M}_\odot$ (Crowther et al. 2010), and it remains unclear if such large mass can be reached by accretion alone in spite of these strong feedback effects. Massive stars appear predominantly in denser clusters than low-mass stars, and massive stars more frequently occur in binary and small-multiple systems (Preibisch et al. 2001; Shatsky & Tokovinin 2002; Lada 2006). Furthermore, recent theoretical (Krumholz & McKee 2008), numerical (Krumholz et al. 2010) and observational (López-Sepulcre et al. 2010) evidence indicate a minimum prestellar core surface density for high-mass star formation, giving rise to a specific environmental dependence that distinguishes the case of massive star formation.

In this paper we present a series of AMR radiation-hydrodynamic simulations of the collapse of massive star forming clouds using the ORION code (Truelove 1997; Truelove et al. 1998; Klein 1999; Krumholz et al. 2007b). These simulations are the first to simultaneously include radiation and protostellar outflow feedback, and to study their interaction. This work is complementary to that of Peters et al. (2010), which included the effect of photoionization but not of radiation pressure or outflows. To probe the environmental dependence for massive star formation, we examine the effect of outflows in star forming cores at several surface densities representative of typical massive star forming regions in the Milky way to regions characteristic of extragalactic super star clusters. To isolate the effect of outflow feedback alone, we include one model where outflows have been turned off in an otherwise identical cloud. In §2 we describe the simulation methodology and input parameters, in §3

the numerical results are presented and discussed and in §4 we summarize the conclusions that can be drawn from the models.

2. Simulation Setup

2.1. Initial Conditions

Our simulations are initialized to the state of a prestellar core of mass M, each with a power law density profile given by

$$\rho(r) \propto r^{-k\rho}, \tag{1}$$

with $k_\rho = 3/2$, consistent with models (McKee & Tan 2002, 2003) and observation (Beuther et al. 2007), and an initial temperature $T_c = 20$ K. The average density, initial radius and free-fall time of the initial core is set by the initial core surface density Σ as

$$\rho_c = \sqrt{\frac{9\pi\Sigma^3}{16M}} \tag{2}$$

$$r_c = \sqrt{\frac{M}{\pi\Sigma}} \tag{3}$$

and

$$t_{\rm ff} = \left[\frac{\pi M}{64G^2\Sigma^3}\right]^{1/4}. \tag{4}$$

The initial core is placed in the center of a a cubical simulation domain spanning 4 times the core radius i.e., ($L_{\rm domain} = 4r_c$) on each side, so that no part of the initial cloud except gas that is entrained into protostellar winds ever approaches the boundary. The initial core is immersed into a uniform ambient environment with density that is 0.01 times that at the edge of the initial core. Pressure balance between the core and environment is maintained by setting the temperature of the ambient gas to 100 times that at the edge of the initial core, $T_{\rm amb} = 2000$ K. The Planck mean opacity of the ambient gas is set to zero to ensure that it does not cool or radiatively heat the core. The cores are initialized with a turbulent velocity field chosen to put them in approximate balance between gravity and turbulent motions. Three Gaussian random fields are generated with power spectrum $P(k) \propto k^{-2}$ for the three velocity components, each normalized to have an integrated norm of unity over the full spectral range sampled. We set the initial velocity in every cell equal to the components of the Gaussian random field times the one dimensional velocity dispersion,

$$\sigma_v = \sqrt{\frac{GM}{2(k_\rho - 1)r_c}} = \left[\frac{G^2 M\pi\Sigma}{4(k_\rho - 1)^2}\right]^{1/4}, \tag{5}$$

corresponding to the velocity at the surface of a singular polytropic sphere (McKee & Tan 2003). The virial parameter $\alpha_{\rm vir} = 5\sigma_v^2 GM/r_c$ (Bertoldi & McKee 1992) is 5 for $k_\rho = 3/2$, somewhat larger than the value of 15/4 in hydrostatic equilibrium (McKee & Tan 2003). The kinetic energy is therefore initially larger than the gravitational energy, but $\alpha_{\rm vir}$ decreases with time due to the decay of the turbulence. The initial radiation energy density is set to the value for a black-body radiation field with radiation temperature $T_r = 20$ K everywhere.

The earliest stages of high-mass star formation occur in infrared dark clouds (IRDCs) (Rathborne et al. 2007) which are detected in absorption against the mid-infrared galactic background (Perault et al. 1996; Egan et al. 1998). Observations of IRDCs indicate a range of surface density in star forming regions from more tenuous sources with $\Sigma \sim 0.1$ g cm^{-2}, to more typical galactic star formation conditions with $\Sigma \sim 1$ g cm^{-2}, to $\Sigma \sim 10$ g cm^{-2} (Beuther et al. 2002b; Rathborne et al. 2006; López-Sepulcre et al. 2010) or more in extra-galactic super-clusters (Turner et al. 2000; McCrady & Graham 2007). Table 2.1 summarizes the parameters for each of the four computational models presented in this work. The initial conditions for these models have been chosen to study the collapse of galactic IRDCs with high but not atypical mass and surface density. Each of the initial simulation core states are rescaled versions of one another with identical density structure, virial ratio, velocity field and comparable peak resolution in every run. We have compared each of the simulations at equivalent time in units of the free-fall time of the initial cores. The homology between the runs is broken only by the presence or absence of outflows and by radiative effects. This choice of model parameters therefore probes the surface density dependence of radiative feedback effects, and isolates the effects of protostellar outflows by holding all other parameters constant as they are turned on and off.

We have largely followed the approach set forth by Krumholz et al. (2010) in choosing the parameters for the numerical simulations considered here. However, the simulations in this work differ from the earlier work in several ways. First, these simulations use an initial core mass of 300 M$_\odot$ instead of 100 M$_\odot$. This choice was motivated by our desire to study the evolution of high-mass star systems and our expectation that protostellar outflows, which were not considered in the earlier models, will eject a significant fraction of the initial core. Secondly, the lowest initial surface density is $\Sigma = 1.0$ g cm^{-2} instead of $\Sigma = 0.1$ g cm^{-2} as used in the earlier work. This choice is largely motivated by computational constraints. The high flow speeds present in runs with outflows necessitate smaller numerical time steps than for non-outflow runs and thus increase the computational cost. A simulation with $\Sigma = 0.1$ g cm^{-2} would be particularly expensive due to its long free-fall time and the need to advance to these later times with numerical time steps that are limited by the cell crossing time of outflow-ejected gas.

2.2. Refinement and Boundary Conditions

The AMR capabilities of the code track the collapsing cores in three dimensions to grid scales of $\Delta x_L \sim 25$ AU on the finest AMR level. This resolution is achieved by discretizing the physical domain on the coarse onto a base grid of N_0^3 cells. The placement of finer level grids up to the finest level L was determined by the refinement criteria that any gas denser than one half the density at the edge of the initial core be refined by at least one level. Further refinement is also triggered wherever the local Jeans number, $J = \sqrt{G\rho\Delta x^2/(\pi c_s^2)}$ (Truelove et al. 1998), exceeds 0.125, where Δx is the computational cell width on the coarser level, or wherever the local gradient of the radiation energy density $|\nabla E_{\rm rad}|\Delta x/E_{\rm rad}$ exceeds 0.1.

The simulations use a zero velocity gradient outflow boundary condition for the hydrodynamics and Marshak boundary conditions for the radiation energy density with radiation flux at the edge of the computational domain for a 20 K background radiation field. The gravitational potential is specified at the edge of the domain as the sum of the multipole

Table 1. Simulation Parameters

Σ (g cm^{-2})	1.0	2.0	2.0	10.0
wind	on	on	off	on
M ($M_\odot$)	300	300	300	300
r_c (pc)	0.141	0.100	0.100	0.0447
$\bar{n}_H$ (cm^{-3})	7.3×10^5	2.1×10^6	2.1×10^6	2.3×10^7
σ_v/c_s	8.80	10.5	10.5	15.6
$t_{\rm ff}$ (kyr)	50.7	30.2	30.2	9.02
$L_{\rm domain}$ (pc)	0.565	0.400	0.400	0.179
N_0	128	192	192	192
max level	5	4	4	3
Δx_L (AU)	28.4	26.8	26.8	24.0

Note. — Row 1: initial core surface density; Row 2: initial core mass; Row 3: initial core radius; Row 4: initial core velocity dispersion; Row 5: core free fall time; Row 6: linear size of the computational domain,; Row 7: number of cells per linear dimension on the coarsest level; Row 8: maximum refinement level; Row 9: computational resolution on the finest AMR level.

moments of the mass distribution in the computational volume as a function of time up to the quadrupole term. We adopt an equation of state with $\gamma = 5/3$, appropriate for gas too cool for molecular hydrogen to be rotationally excited, but this choice is essentially irrelevant because the gas temperature is set almost purely by radiative effects.

2.3. Optical Properties and Equation of State

The radiation transport is handled by a frequency-integrated flux limited diffusion approximation. We use the Planck and Rosseland mean dust opacities, $\kappa_{\rm P}$ and $\kappa_{\rm R}$ respectively, of the Semenov et al. (2003) iron normal, composite aggregates model plotted in figure 1. The simulations with protostellar winds introduce strong heating behind wind-driven shocks. When the thermal energy of the gas exceeds that of a gas with molecular weight $0.6m_p$ and temperature 10^4 K, we treat the gas as fully ionized with Rosseland opacity $\kappa_{\rm R} = 0.32$ cm^2 g^{-1}, the value for Thompson scattering at solar metallicity. Our gray flux limited diffusion approximation cannot adequately represent the collisionally-excited line cooling processes that dominates at temperatures above the dust destruction temperature. However, it is critical to include them in order to ensure that shocked gas is able to cool. We therefore leave $\kappa_{\rm P} = 10^{-2}$ cm^2 g^{-1} for this gas, ensuring that it does not interact strongly with the ambient radiation field, but we also implement an approximate line cooling function $\lambda(T)$ to remove energy from gas above the dust destruction temperature and transfer it to the radiation field. We take $\lambda(T)$ from the function shown in figure 1 of Cunningham et al. (2006). In each time step, before we perform our ordinary flux limited diffusion radiation solve, we update the gas and radiation energy densities by implicitly solving the operator split-system

$$\frac{d\rho e}{dt} = -(\rho/\mu)^2\lambda(T) \tag{6}$$

$$\frac{dE}{dt} = (\rho/\mu)^2\lambda(T) \tag{7}$$

using the LSODE (Radhakrishnan & Hindmarsh 1993) Gear-type solver. In the above system, e is the specific thermal energy density of the gas, E is the radiation energy density, μ is the mean molecular weight and T is the gas temperature appropriate for a solar metallicity ionized gas mixture.

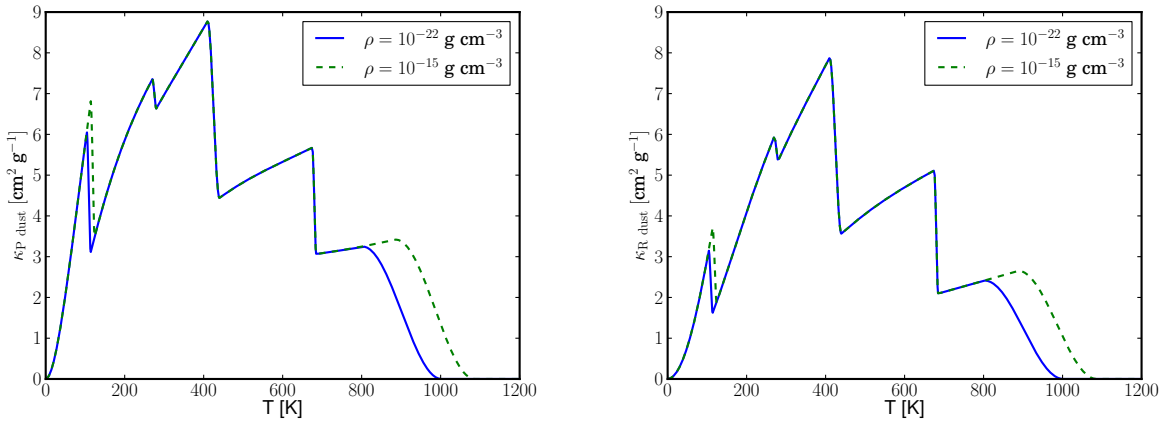

Fig. 1.— Dust opacity model (Semenov et al. 2003). Left: Planck mean dust opacity as a function of gas temperature. Right: Rosseland mean dust opacity.

2.4. Protostellar Wind Model

The ORION code includes a "star particle" algorithm to handle the formation of protostars (Krumholz et al. 2004, 2007a). This algorithm provides for the creation of sub-grid star particles in those cells of the computation that become poised for gravitational collapse to spatial scales smaller than those that can be captured on the computational grid without spurious fragmentation (Truelove et al. 1997). The luminosity, radius and burning state of the star particle is advanced with the simulation according to the protostellar evolution model of McKee & Tan (2003) as updated by Offner et al. (2009). The protostellar luminosity prescribed by this model enters the simulation as a source term in the radiation energy density equation.

The ORION star particle algorithm has been enhanced for this work to include the driving of bipolar outflows. Our outflow model is specified by the dimensionless parameters f_w and f_v, which set a wind launch speed as a fraction f_v of the Kepler speed at the stellar surface and a mass flux that is a fraction f_w of the rate of accretion onto the star or, equivalently, a fraction $f_w/(1+f_w)$ of the total mass that is either accreted onto the star or ejected in the wind. The wind driving is imposed by operator split source terms in the gas density, momentum density and energy density equations with

$$\left.\frac{d\rho}{dt}\right|_s = -\dot{M}_{w,i}\ \chi_w(|\mathbf{r}_i|)\ \bar{\xi}(\theta_i), \tag{8}$$

$$\left.\frac{d\rho\mathbf{v}}{dt}\right|_s = -f_v v_{k,i}\ \dot{M}_{w,i}\ \chi_w(|\mathbf{r}_i|)\ \bar{\xi}(\theta_i)\ \cdot \hat{\mathbf{r}}_i, \tag{9}$$

$$\left.\frac{d\rho e}{dt}\right|_s = -\dot{M}_{w,i}\ \chi_w(|\mathbf{r}_i|)\ \bar{\xi}(\theta_i)\ \frac{k_B 10^4\ \mathrm{K}}{\mu(\gamma-1)}, \tag{10}$$

where $v_{k,i} = \sqrt{GM_i/r_{*,i}}$ is the Keplerian speed at the surface of the star and $r_{*,i}$ is the protostellar radius of McKee & Tan (2003). The corresponding rate of particle mass growth, particle wind mass ejction rate, acceleration, radial distance and spatial inclination of the ith star are

$$\dot{M}_i = \frac{1}{1+f_w}\dot{M}_{KKM04}, \tag{11}$$

$$\dot{M}_{w,i} = f_w\dot{M}_i = \frac{f_w}{1+f_w}\dot{M}_{KKM04}, \tag{12}$$

$$\dot{\mathbf{v}}_i = \dot{\mathbf{v}}_{KKM04}, \tag{13}$$

$$\mathbf{r}_i = \mathbf{x} - \mathbf{x}_i, \tag{14}$$

$$\theta_i = \mathrm{acos}(\hat{\mathbf{r}}_i \cdot \hat{\mathbf{j}}_i) \tag{15}$$

where $\mathbf{j}_i$ and $\mathbf{x}_i$ are the velocity and position of the ith particle, $\mathbf{j}_i$, $\dot{M}_{KKM04}$ and $\dot{\mathbf{v}}_{KKM04}$ are the sink particle angular momentum, accretion rate and acceleration for the case in which winds are absent as given by the algorithm of Krumholz et al. (2004). The X-wind (Shu et al. 1988) and disk wind (Pelletier & Pudritz 1992) theoretical models provide some guidance as to the mass ejection rate of $f_w \sim 1/3$ and $f_w \sim 0.1$ respectively. Our choice of model parameters is further guided in terms of momentum injection by observations of low-mass stars. Richer et al. (2000) extract a fiducial protostellar momentum flux of $f_w f_v \sim 0.3$. For $v_k \approx 200$ km s^{-1} this implies a net wind momentum of $\sim 60\mathrm{M}_\odot$ km s^{-1}, although this has significant uncertainties. Wind launch speeds represent the Courant time-step constraint in a typical calculation, so large values of f_v impose a particularly onerous computational burden. We therefore choose a wind mass to stellar mass fraction on the high end of the theoretical guidance, $f_w = 0.27$ and the wind velocity parameter toward the low end of the observed momentum range, $f_v = 1/3$. The net momentum injected by our wind model is therefore characterized by $f_w f_v = 0.09$, which, given the uncertainties, is within the observed range of rates of momentum injection by outflows.

The function

$$\chi_w(r) = \frac{1}{C_1}\begin{cases} r^{-2} & \text{if } 4\Delta x < r \le 8\Delta x \\ 0 & \text{otherwise} \end{cases} \tag{16}$$

is a normalized weighting kernel that determines the spatial scale of the wind injection where C_1 is a normalization constant to the weighting kernel. The C_1 is computed numerically in the ORION code so that numerical aliasing effects of the spherical wind injection region into the Cartesian grid are accounted for exactly.

The remaining function $\bar{\xi}$ describes the angular distribution of the wind mass and momentum flux at the point where it is injected into the computational grid. We take this function from Matzner & McKee (1999), who find that the momentum distribution of prestellar outflow injection asymptotically far away from the protostellar surface as a function of the polar angle θ from the direction of the protostar's rotation is given by

$$\xi(\theta, \theta_0) = \left[\ln\left(\frac{2}{\theta_0}\right) (\sin^2\theta + \theta_0^2) \right]^{-1} \tag{17}$$

where θ_0 is the so called "flattening parameter" that sets the opening angle of the wind. In the case of low-mass stars, Matzner & McKee (1999) suggest a fiducial value of $\theta_0 = 0.01$ and we adopt the same value here. While stars of type B or later direct momentum in a very well-collimated beam (Beuther et al. 2002a, 2003, 2004), O star winds are collimated somewhat more weakly, possibly due to the effect of ionization (Beuther & Shepherd 2005). Since we do not include ionizing radiation in these simulations, we do not attempt to model to model O star wind broadening.

The large value of ξ near $\theta = 0$ in equation (17) requires particular care in implementing this model in a numerical code. We implement the driving function by averaging ξ over the polar angle subtended by a grid cell $\Delta\theta = \mathrm{atan}(1/8)$ at the outer radius of the weighting kernel (equation (16)) as

$$\bar{\xi}(\theta, \theta_0) = \frac{1}{C_2} \begin{cases} \frac{1}{\Delta\theta} \int_{\theta-\Delta\theta/2}^{\theta+\Delta\theta/2} \frac{d\theta}{\sin^2\theta + \theta_0^2} & \text{if } |\sin(\frac{\pi}{2} - \theta)| \geq \frac{\Delta x}{r} \\ 0 & \text{otherwise.} \end{cases} \tag{18}$$

Our choice to set $\bar{\xi}$ to zero for angles close to $\pi/2$ is driven by numerical considerations. If we allow the outflow to be injected into 4π steradians around the star, its mass and momentum are sufficient to disrupt the early development of an equatorial disk. This behavior is an artifact of the necessarily poor resolution inside the wind launching region. We do not resolve the disk scale height, and this artificially puffs up the disk and reduces its mass and momentum density, rendering it far easier for the outflow to disrupt than it would be if its true scale height were resolved. We avoid this problem by reducing the outflow mass and momentum flux to zero in an equatorial belt that is at least one cell thick, ensuring that accreting material always has an uninterrupted path to the star.

The definite integral in equation (18) evaluates to

$$\int_{\theta-\Delta\theta/2}^{\theta+\Delta\theta/2} \frac{d\theta}{\sin^2\theta + \theta_0^2} = \frac{1}{\theta_0\sqrt{\theta_0^2+1}} \left[\mathrm{atan}\left(\frac{\sqrt{\theta_0^2+1}\tan\left(\theta + \frac{\Delta\theta}{2}\right)}{\theta_0} \right) - \mathrm{atan}\left(\frac{\sqrt{\theta_0^2+1}\tan\left(\theta - \frac{\Delta\theta}{2}\right)}{\theta_0} \right) \right] \tag{19}$$

The normalization constant $C_2 = \int \xi(r,\theta)\chi_w(r)d^3\mathbf{x}$ is also computed numerically to exactly account for grid alliasing effects. Neglecting the grid aliasing effect, we find $C_2 = 65.7$ by numerical integration. A second subtlety that arises in the numerical implementation of the wind driving is that care must be taken so that the momentum source terms impart exactly zero net momentum onto the star particles and the gas in the computational domain. If the position of the particle is allowed to vary continuously within its host cell the $\frac{1}{r^2}$ term in equation (16) may lead to an asymmetric driving. To overcome this problem, we bring the wind driving into symmetry with the numerical grid by rounding the particle position to the nearest half-integer multiple of the grid width

$$\mathbf{x_i} \leftarrow 2\Delta\mathbf{x}\ \mathrm{nint}\left[\frac{\mathbf{x_i}}{2\delta\mathbf{x}}\right] \tag{20}$$

before computing the source terms (equations (11-9)) where nint is the "nearest integer" function.

The wind momentum injection $\bar{\xi}$ is significantly broadened at polar latitude relative to the analytic prescription for ξ. Consequently less momentum is injected near the equator to satisfy the normalization constraint. To facilitate comparison of our numerical models with the analytic predictions of Matzner & McKee (2000) in §3.5 it is convenient to define the effective numerical flattening parameter $\theta_{0,\mathrm{eff}}$ at large angle as:

$$\xi(\theta, \theta_0 = \theta_{0,\mathrm{eff}}) = \bar{\xi}(\theta, \theta_0 = 0.01). \tag{21}$$

We find that the above expression holds to within 1% for $\theta > 32^\circ$ with $\theta_{0,\mathrm{eff}} = 5.75 \times 10^{-4}$.

3. Results

3.1. Large-Scale & Outflow Morphology

The left column of figures 2 through 5 show the large scale evolution of each simulation from $t = 0.2t_{\mathrm{ff}}$ to $t = 0.8t_{\mathrm{ff}}$ in increments of $0.2t_{\mathrm{ff}}$. These plots show slices of density with the color-mapping scaled by $\Sigma^{3/2}$ following the scaling given in equation (2). The spatial scale shown in each plot scaled by the initial core radius with each showing an area $(2.5r_c)^2$. The slices are centered on the position of the primary protostar and oriented so that the angular momentum vector of the protostar is upwardly oriented on the page. As expected, once the scaling of cloud radius and surface density is accounted for, the regions that have not been penetrated by the outflow bow shocks collapse in a homologous manner with little dependence on the initial surface density. The protostellar outflows evacuate a shock-bounded cavity through the initial cores and the outflow cavities are the prominent features in the density

slices in the left column by $t \sim 0.3t_{\rm ff}$ in the lower surface density cases and $t \sim 0.4t_{\rm ff}$ in the high surface density case. The propagation speed of the outflow bow shocks through the core and the width of the outflow cavities show a strong dependence on initial surface density. The lower surface density cores show significantly greater disruption due to the protostellar outflow feedback. This effect is due to 1) greater mechanical luminosity of the protostellar winds at lower surface density (an effect that we discuss in detail in §3.3 and 2) lower turbulent ($\sigma_v^2 \propto \Sigma^{1/2}$) and thermal pressures ($P_c \propto \rho_c T_c \sim \Sigma^{3/2}$) in the ambient cores which act to confine the propagation of the outflows. We note that the outflow-evacuated cavities in the cases with outflows emerge from the initial core toward the left side of the density slices in figure 5. The reason for this is that the primary star particle retains the momentum of the material that it accretes and therefore the star drifts away from the center of mass of the initial core with time (see §3.3). The outflowing material therefore emerges first from the thinnest side of the initial cloud, relative to the position of the primary star.

3.2. Fragmentation & Star Formation

The third column of figures 2 through 5 show the small scale evolution of the surface density. Each of the plots are scaled by the initial surface density Σ and the initial core radius, with each showing an area $(0.1r_c)^2$ centered on the position of the primary star. Deviations from the the homologous scaling with surface density exhibited on larger scales appear by $t = 0.2t_{\rm ff}$. The simulations with higher initial surface density are characterized by higher surface density disks, even when normalized by the initial surface density. By $t = 0.4t_{\rm ff}$ in figure 3 and $t = 0.6t_{\rm ff}$ in figure 4, notable differences in the disk around the primary protostar emerge. Progressing from the third row, showing the case with highest surface density, to the top row, showing the case of lowest surface density we note an increasing tendency of the disk around the primary star to fragment and generate spiral arms characteristic of a Toomre-unstable disk (Toomre 1964). In the simulations with lower surface densities in the top two rows of figure 4) we note a prominent increase in disk fragmentation in terms of the multiplicity of star particles and the presence of distinctly separate accretion disks around the primary and secondary protostars in comparison to the highest surface density case in the third row.

The trend toward reduced disk stability and enhanced fragmentation with lower initial surface density is consistent with earlier analytic (Krumholz & McKee 2008) and numerical (Krumholz et al. 2010) works that predict a threshold core surface density for sufficient radiative heating to inhibit disk fragmentation of $\Sigma \sim 1.0$ g cm^{-2}, as well as with observational data from infrared star-forming clouds that are consistent with this prediction

(López-Sepulcre et al. 2010). We will show in §3.4 that protostellar outflows provide a mechanism for focusing radiative feedback in the poleward directions, away from the the infalling disk in the midplane, as predicted by Krumholz et al. (2005). Protostellar outflows should therefore raise the surface density threshold for high-mass star formation. The simulations presented here do not survey sufficiently low surface densities to quantify this effect, due to the computational cost of simulating protostellar winds inside low surface density cores with commensurately longer free fall times. Furthermore, we expect that the relative importance of this effect may depend on magnetic fields, which our simulations neglect, and their role in confining the outflow cavity (Hennebelle et al. 2011). We therefore defer more precise quantification of the effect of outflows on the minimum surface density threshold for high-mass star formation to future work that will include magnetic fields and survey lower surface density cores.

We can isolate the effect of protostellar outflows on the small-scale evolution by comparing the second and fourth rows of figures 2 through 5 which show the results of our numerical experiments with and without protostellar outflow ejection, both with the same initial surface density of $\Sigma = 2.0$ g cm^{-2}. By $t = 0.4t_{\rm ff}$ enhanced radiation trapping in the case with outflows has lead to substantially warmer circumstellar gas in comparison to the case without outflows. The temperature structure in the $\Sigma = 2.0$ g cm^{-2} case *without* protostellar outflows in the fourth row is more similar to the $\Sigma = 10.0$ g cm^{-2} case *with* outflows in the third row than to the case at the same surface density with winds in the second row. As we will show in §3.4, protostellar outflow cavities carve a path of reduced optical depth through the initial core that channel radiative flux away from the center of the core. This escape of radiative energy reduces the efficacy of radiative heating in the central regions of the collapsing core.

Enhanced disk fragmentation associated with outflows and decreasing surface density is due to the reduced effectiveness of radiative heating. The right columns of figures 2 through 5 show the mass-wighted, column-averaged radiation temperature T_r over the same regions as the column density projections in the center column. We note that the dense infalling gas is strongly coupled to the radiation field, so that the gas temperature $T \approx T_r$. Only the tenuous outflow-evacuated regions achieve sufficient post-shock temperatures to break the radiation-gas coupling by increasing the gas temperature beyond the dust destruction temperature. The column-averaged radiation temperature plots therefore allow us to probe the temperature structure of the dense infalling gas without confusion from the projection of shock heated layers along the surfaces of the outflow cavity. The temperature structure of the gas on small scales shows even stronger dependence on the initial surface density than the column density. We note enhanced temperature with increasing surface density as early as $t = 0.2t_{\rm ff}$ when no stars are producing significant power via nuclear burning. The dependence

of temperature on surface density at these times is solely due to the factors pointed out by Krumholz & McKee (2008); (1) Higher surface density cores have higher accretion rates, thereby generating higher accretion luminosity and (2) higher surface density cores have higher optical depth to more effectively trap radiation. The trend toward increasing gas temperature with increasing surface density is also present at all later times, due to additional radiative output from nuclear burning in the primary star in addition to enhanced accretion luminosity and enhanced radiative trapping.

Stars with masses $\gtrsim 15 M_\odot$ generate sufficient radiation pressure to exceed their gravitational acceleration. The second column of figures 3, 4 and 5 show that by then the spherically-averaged radiation force from the central protostar exceeds the inward gravitation attraction acting on the dusty envelope of infalling gas in the case of $\Sigma = 10.0$ g cm^{-2} and in the case of $\Sigma = 2.0$ g cm^{-2} without outflows. In the case without outflows this strong radiative force drives the expansion of a bubble of circumstellar gas away from the central source. The early development of this bubble can be see in the lower left panel of figure 3 at $t = 0.4t_{\rm ff}$ and the radial extent of the bubble grows to a size scale comparable to that of the initial core by $t = 0.8t_{\rm ff}$ as shown in figure 5. The radiation bubble emerges from the initial core on the left side of the density slices in figure 5. This is due to the drift of the primary star away from the center of mass of the initial core with time. The radiation bubble emerges first from the thinnest side of the initial cloud, relative to the position of the primary star. Accretion onto the primary star continues through the radiatively supported bubble via Rayleigh-Taylor unstable modes (Krumholz et al. 2009; Jacquet & Krumholz 2011) that develop dense, radiatively self-shielding spikes of infalling gas. The evolution of radiative bubbles in similar simulations without winds and without initial turbulence are discussed in detail by Krumholz et al. (2009). The sole difference between the radiation bubbles presented here and those in the earlier work is that the bubbles presented here are considerably less symmetrical about the central source owing the the turbulent ambient environment.

In the case with winds, the regions where the net force is dominated by the outward radiation force lie within the outflow cavity. These regions are dominated by outflow irrespective of the radiation force. With protostellar outflow, in no case does radiation force exceed that of gravity acting on the infalling core gas. Consequently, no such radiation supported bubbles form in any of the models with protostellar winds. As predicted in Krumholz et al. (2005), the cavities evacuated by protostellar outflows provide sufficient focusing of the radiative flux in the poleward directions that accretion continues through the regions of the infalling envelope onto the disk that are not disrupted by the protostellar wind shocks, and the infalling motion of this gas is not interrupted by the effects of radiation pressure.

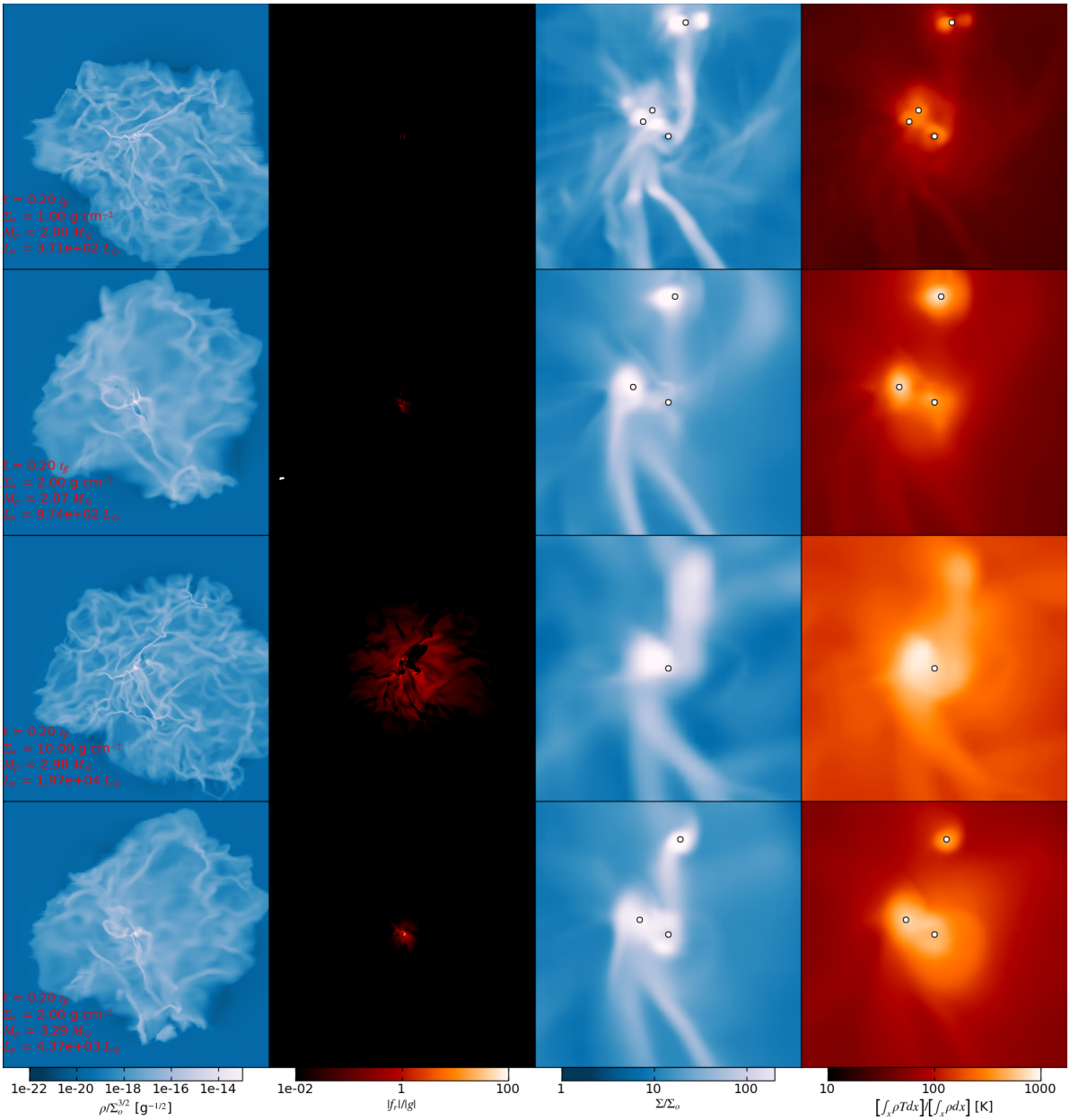

Fig. 2.— Simulation graphics at $t = 0.2t_{\rm ff}$ for the parameters $\Sigma = 1.0$g cm^{-2}, $\Sigma = 2.0$g cm^{-2}, $\Sigma = 10.0$g cm^{-2}, and $\Sigma = 2.0$g cm^{-2} (without winds) from top to bottom. First column: $\rho/\Sigma^{3/2}$ on a $(2.5r_c)^2$ plane oriented so that the outflow launch direction lies in the plane of the image, pointing toward the top of the page. Second Column: Ratio of the radiation force magnitude to gravitational force magnitude. Third Column: Column density on a $(0.1r_c)^2$ plane aligned with the cardinal axes of the simulation, oriented so that the primary protostellar outflow direction is as close as possible to pointing vertically out of the page. Fourth Column: Mass-weighted radiation temperature projected in the same manner as the surface density in the third column. All plots are centered on the projected position of the primary star. White markers indicate star particles.

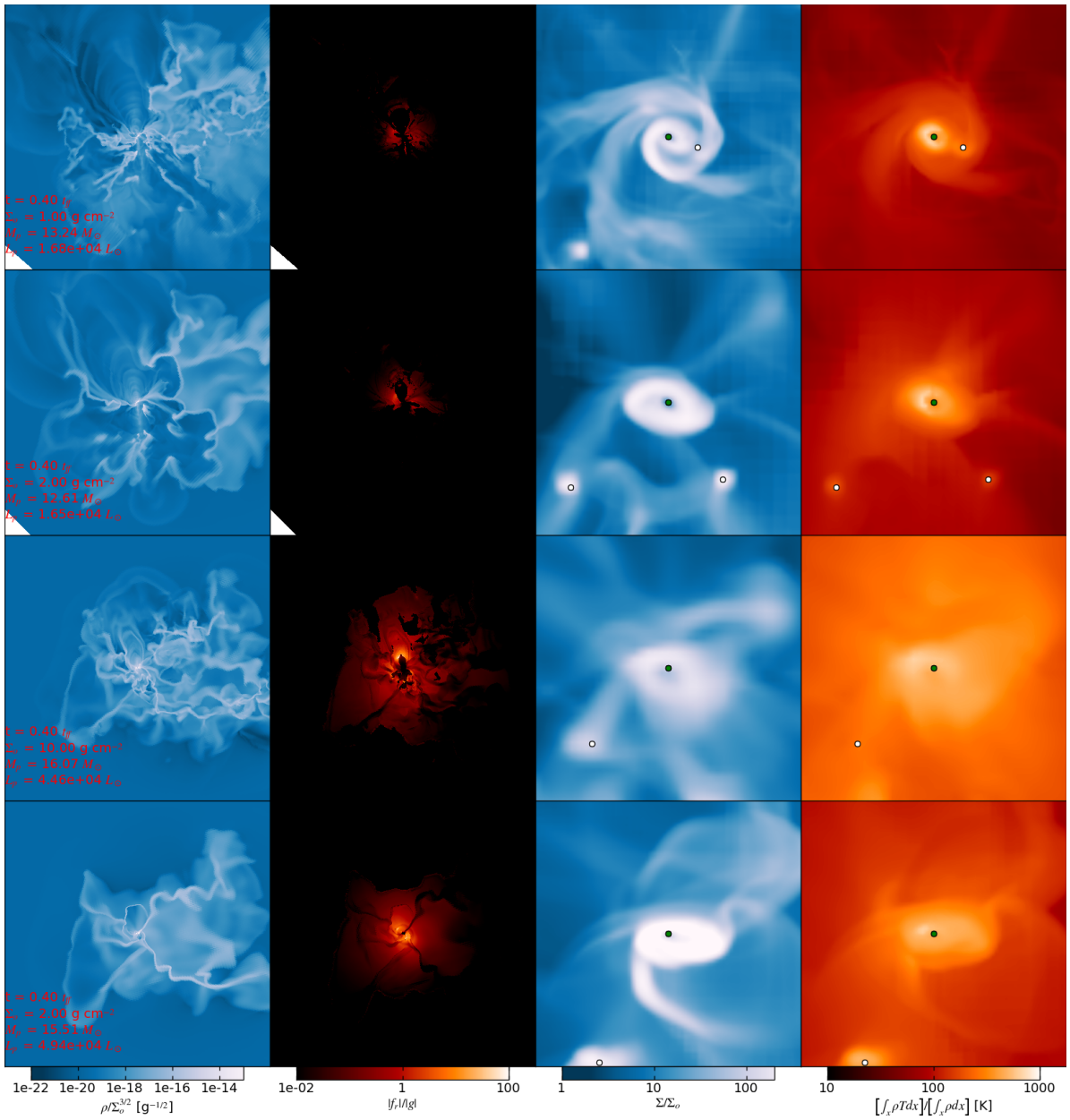

Fig. 3.— Same as figure 2 but at $t = 0.4t_{\rm ff}$.

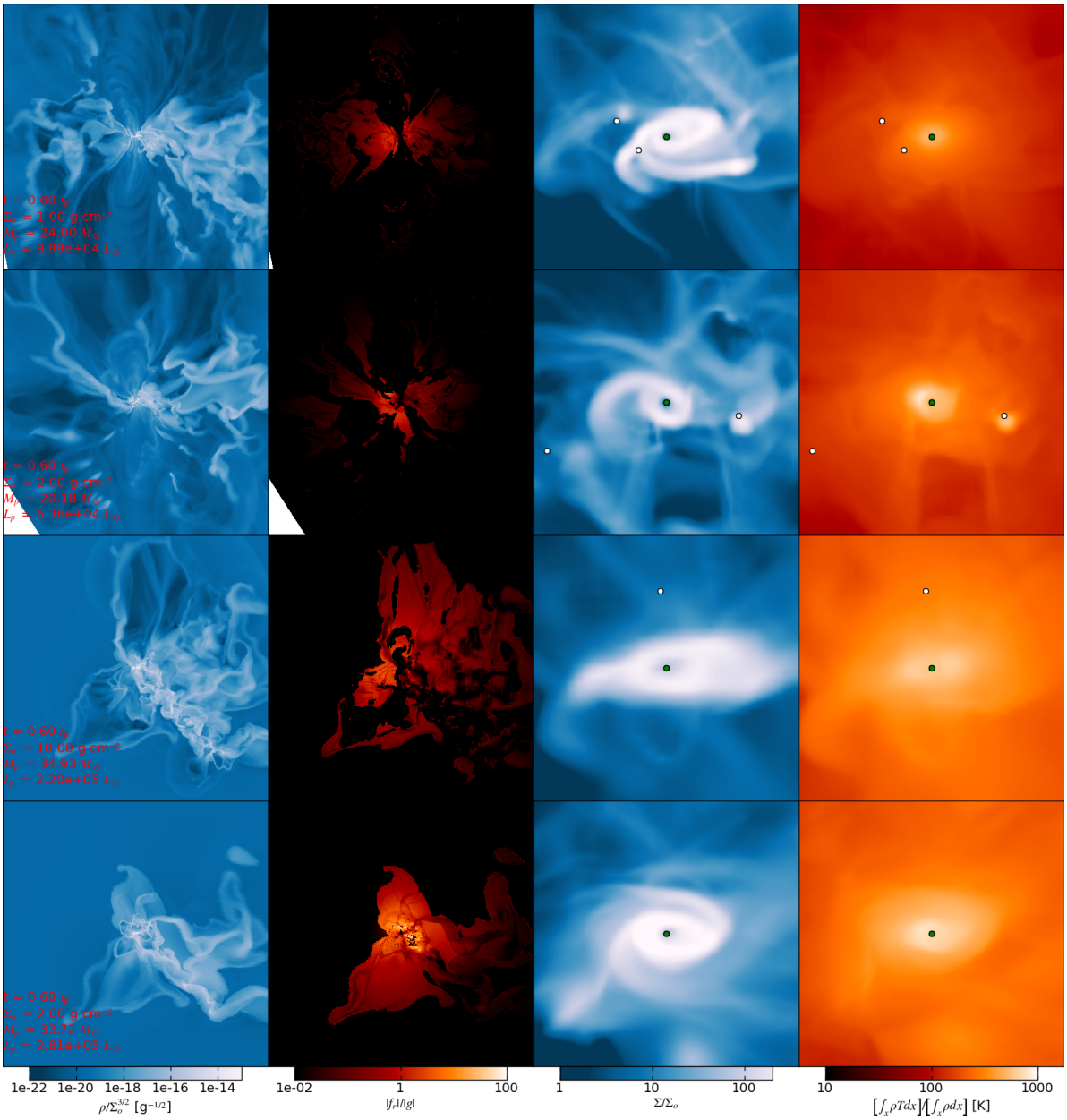

Fig. 4.— Same as figure 2 but at $t = 0.6t_{\rm ff}$.

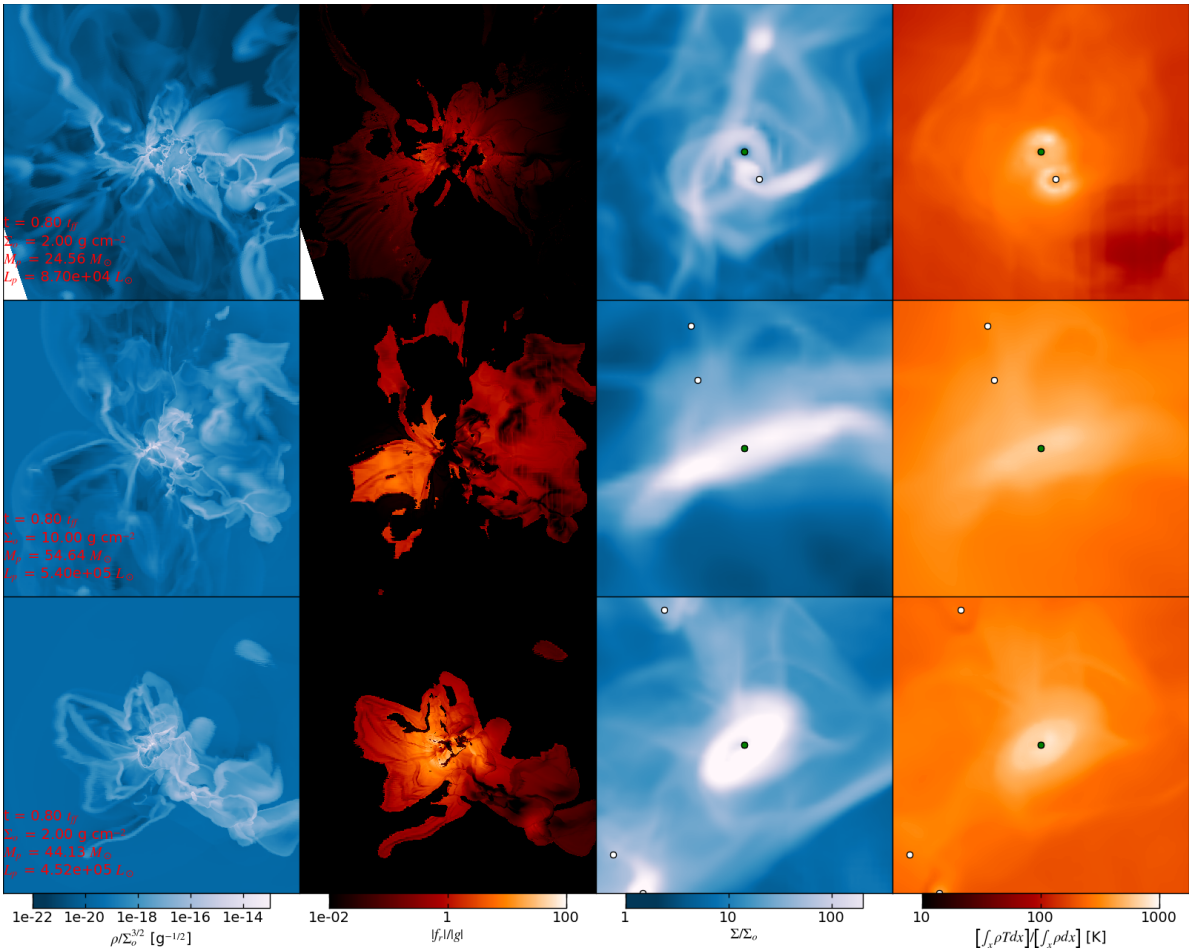

Fig. 5.— Same as figure 2 but at $t = 0.8t_{\rm ff}$. Only the surface density parameter cases of $\Sigma = 2.0$g cm^{-2}, $\Sigma = 10.0$g cm^{-2}, and $\Sigma = 2.0$g cm^{-2} (without winds) were run to this time.

3.3. Protostar Properties

The upper left panel of figure 6 shows the time dependence of mass accretion onto star particles for each simulation and the middle left panel shows the time dependence of mass accretion onto the primary protostar. Abrupt jumps in the primary protostellar mass occur due to the merger of other particles that fall toward the primary star. The code has been constructed to merge star particles that cannot be resolved on the resolution scale of four computational zones on the finest level (see Krumholz et al. (2004)). Because these mergers are resolution-dependent effects, we have taken care to assure that the mass contribution to stellar sources due to mergers is small. As we have discussed earlier, the ambient core in the case of $\Sigma = 1.0$ g cm^{-2} is subject to the least efficient radiative heating and is the most susceptible to gravitational fragmentation and therefore the most difficult to resolve. The particle mergers account for $\sim 15\%$ of the total primary protostellar mass by the end of the simulation in the $\Sigma = 1.0$ g cm^{-2} case and about $\sim 10\%$ in the higher surface density cases. Most of the mass accumulated by merger events in the case of $\Sigma = 1.0$ g cm^{-2} occurs due to the merger of a secondary star particle of $3.0\mathrm{M}_\odot$ at $t = 0.52t_{\mathrm{ff}}$. We do note, however, that Myers et al. (2011) have found that imposing a maximum mass threshold for mergers enhanced fragmentation and limited the rate of mass growth of the primary star in more highly resolved but otherwise similar simulations. We therefore regard the stellar mass predictions in the models presented here as an upper limit. In comparing the cases with protostellar outflows we note that the total system mass in stars, M, exhibits a weak trend toward more rapid accretion with higher surface density even when the time is scaled by the free-fall time. In other words, $\dot{M}t_{\mathrm{ff}}$ increases weakly with the surface density of the initial core, Σ. This is because outflows entrain and unbind less gas from the ambient core in cases with higher surface density. Therefore, the luminosity output from the more massive protostars is enhanced in the higher surface density cases. This contributes to more effective heating and decreased fragmentation of the ambient core in the higher surface density cases as noted in §3.2. Consequently, the simulations at lower surface density fragment into low multiple systems earlier and are characterized by significantly reduced accretion to the primary star in comparison to the models at higher surface density.

The upper right and middle right panels of figure 6 show the stellar luminosity and the speed of the protostellar wind driving from the primary protostar as a function of time. Nuclear burning dominates the radiative output from stars with mass exceeding $5\mathrm{M}_\odot$ and the primary protostar dominates the stellar feedback into the core. The rapid increase in mechanical feedback from winds in all of the models is driven by the Kelvin-Helmholtz contraction of protostar (Shu et al. 1987). Stellar contraction causes the escape speed at the protostellar surface to increase which in turn increases the wind ejection speed with $v_w = v_{\mathrm{esc}}/3$ (see §2.4). By $t = 0.2t_{\mathrm{ff}}$ all of the models have undergone sufficient contraction

to ignite deuterium burning in the stellar cores, leading to a rapid increase in luminosity. Rapid contraction of the stellar surface continues as deuterium is exhausted in the prestellar core, giving rise to a commensurate increase in wind speed from $t = 0.2t_{\rm ff}$ to $t = 0.3t_{\rm ff}$.

Contrary to the increase in the effects of radiative feedback with surface density, we find that the effects of mechanical feedback on the ambient cores decrease with the initial surface density. For $t > 0.4t_{\rm ff}$ the primary wind speeds show a noticeable decrease with increasing surface density. This occurs due to a mismatch between the Kelvin time for the contraction of the stellar surface and the free-fall time of the ambient molecular cloud core. The former depends mostly on the protostellar mass whereas the latter scales as $t_{\rm ff} \propto \Sigma^{-3/4}$ (equation (4)). This means that lower surface density simulations form stars that undergo more rapid Kelvin contraction *per unit free-fall time* and thereby eject more powerful winds at equivalent stages of collapse. We note that this result is driven by the assumption built into our numerical model that the wind ejection speed is proportional to the escape speed at the protostellar surface. As discussed in §3.2, the more powerful winds contribute to the enhanced disruption of the ambient core in the lower surface density simulations. However, the overarching trend toward enhanced disruption of the ambient core with lower surface density would remain even if the wind speed as a function of core free-fall time were independent of surface density. First, the outflow break-out time from the core, $t_{\rm outflow} = r_c/v_w$ would scale, relative to the free-fall time, as $t_{\rm outflow}/t_{\rm ff} \sim \Sigma^{1/4}$, resulting in later outflow emergence from higher surface density cores. Second, higher surface density cores enhance the confinement of outflow cavities due to higher ambient pressures.

The cascade of turbulent motions through the collapsing cloud strongly affects the motion of the primary star as a function of time. The lower left panel of figure 6 plots the distance between the primary star, at position $\mathbf{r_p}$, and the center of mass of the system, at position $\mathbf{r}_{COM}$. The drift of the primary star away from the center of the system is a result of the random velocity field. Because most of the turbulent energy is in large wavelength modes, the denser center of the cloud will tend to have a different velocity than the lower density edges. As a result the location of the star drifts from where it first forms.

The cascade of turbulent motions through the collapsing cloud also strongly affect the orientation of the primary star as a function of time. The lower right panel of figure 6 shows the angle of inclination of the angular momentum accreted by the primary protostar particle relative to the $\hat{\mathbf{z}}$ direction. We note that the total angular momentum of the initial cloud has an orientation that is inclined 27° to the $\hat{\mathbf{z}}$ direction. Because no radiative heating feedback is present in the initial state of the cloud, the early evolution of the simulations are characterized by fragmentation of the densest portion of the initial cloud into 2 to 4 gravitationally bound particles, as shown in figure 2. By $t = 0.3t_{\rm ff}$, the radiative feedback

from the primary star is sufficient to suppress local fragmentation and the initial fragments merge. The angular momentum of the primary particle at early time varies over $\sim 90°$ as a consequence of variation in the angular momentum of the surrounding gas and as a consequence of the coalescence of the initial fragments. After $t = 0.3t_{\rm ff}$ the primary star has built up a sufficient moment of inertia relative to the rate of angular momentum deposition by accretion that the orientation of the star changes less rapidly. Subsequent evolution ($t = 0.3t_{\rm ff}$ to $t = 0.8t_{\rm ff}$) of the orientation of the primary star is characterized by a rotation of 20° to 40°. We note that the change in angular momentum in the lower surface density cases ($\Sigma = 1.0$ g cm^{-2} and $\Sigma = 2.0$ g cm^{-2}) occurs in abrupt jumps, whereas the higher surface density case is less susceptible to numerical fragmentation and therefore are characterized by relatively smoother change.

The cumulative distribution of stellar masses at $t = 0.5t_{\rm ff}$ for each of the runs shown in figure 7. Both the highest surface density case with $\Sigma = 10.0$ g cm^{-2} and the case without outflows at surface density $\Sigma = 2$ g cm^{-2} collapse to a single star of 70% of the total mass accreted, consistent with the qualitative similarity in the small-scale temperature structure noted in §3.2. The lower surface density cases on the other hand fragment into binary systems with > 1 M$_\odot$ secondaries present by $t = 0.4t_{\rm ff}$. These results demonstrate that the absence of outflows and/or higher initial surface densities result in less fragmentation and the production of fewer, more massive stars.

3.4. Radiation Focusing

The radiative feedback from stellar sources into the ambient cloud is not isotropic. Four possible causes of anisotropic stellar output include (1) the clearing of an optically thin outflow-swept cavity along the poles of the star, (2) shielding in the midplane due to the presence of an optically thick accretion disk, (3) non-uniform optical thickness of the ambient cloud due to the displacement of the star relative to the center of mass of the ambient cloud, and (4) non-uniform optical thickness of the ambient cloud due to the turbulent density structure. In this section we consider the distribution of radiative output from the primary star in each simulation as a function of solid angle to elucidate the importance of each of these effects in shaping the radiative feedback into the ambient cloud.

Figure 8 shows the radiative flux from the primary protostar as a function of spherical angle in each model at times $t = 0.3,\ 0.4,$ and $0.6t_{\rm ff}$, normalized to the radiative flux that would be expected in an isotropic environment $\mathbf{F}_{\rm isotropic} \cdot \hat{\mathbf{r}} = L_p/(4\pi r^2)$. The plots shown in figure 8 have been constructed from slices of the radial radiation flux at a distance of 1500 AU from the primary star, rotated into the coordinate system where the angular momentum of

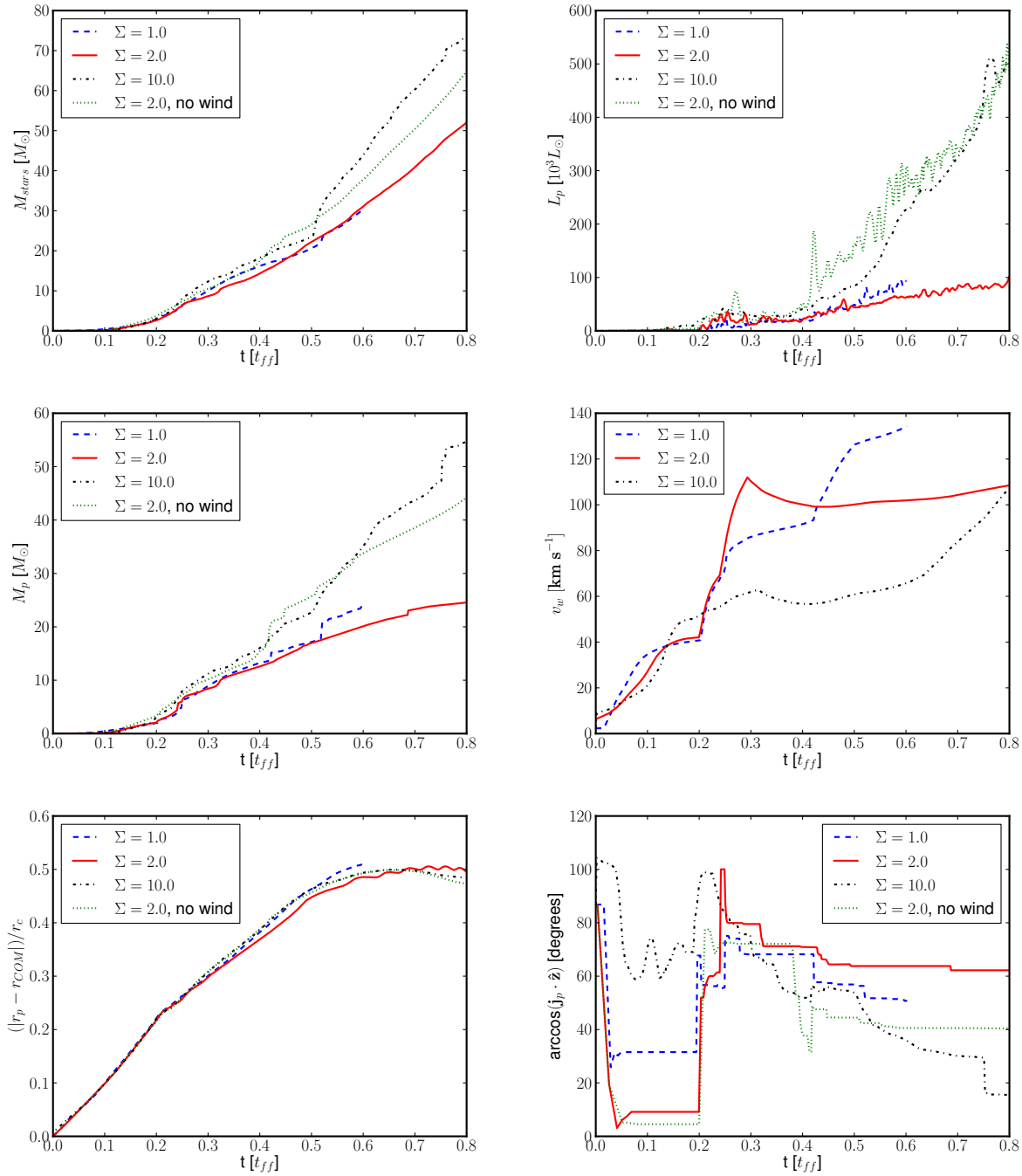

Fig. 6.— Stellar properties as a function of time for each set of simulation parameters. Upper Left: Total mass in stars. Upper Right: Primary star luminosity. The luminosity has been smoothed using a 200 yr moving average to eliminate the high frequency contribution of the accretion luminosity in this plot. Middle Left: Primary star mass. Middle Right: Primary protostellar wind speed. Lower Left: Position of the primary star relative to the center of mass of cloud. Lower Right: Angle between the primary star's angular momentum vector and the z-axis.

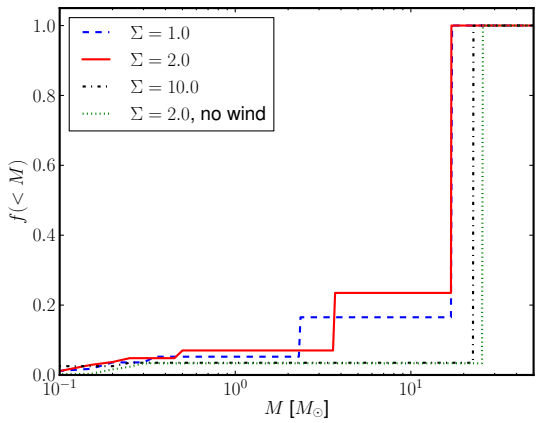

Fig. 7.— Fraction $f(< M)$ of total stellar mass contained in stars with mass $< M$ as a function of the total mass in stars for each of the runs at time $t = 0.5t_{\rm ff}$.

the primary star points upward. The angular distribution of the radiative flux is relatively insensitive to the position of the spherical slice, provided that the slice has radius greater than that of the disk around the primary protostar. In varying the radius of the spherical slice from 1500 AU to 10^4 AU, we note a decreased contrast between regions of low and high radial flux by about $\sim 25\%$, which we attribute, in part, to the flux limited diffusion approximation used for the radiation transport. However, the location and extent in solid angle of the large-scale features is independent of the position of the slice. The azimuthal coordinate facing the thinnest edge of the cloud due to the motion of the star relative to the center of mass of the system is centered in each of the plots. Regions of peak outward radiative flux correlate very well with outflow ejection, and regions of low outward radiative flux correlate very well with the presence of the accretion disk near the midplane. The clearing of low optical depth paths of escape by outflow ejection and shielding by the dense accretion disk in the midplane are therefore the dominant effects in focusing the radiative feedback from the star. As gas falls in toward the primary protostar, it carries its angular momentum with it. In the highest surface density gas the accretion flow is fairly smooth because radiative heating raises the pressure near the primary star and prevents gas around it from clumping up. At lower surface densities, however, the accreting gas may be partially collapsed under its own gravity, or may even have collapsed completely to form stars that then merge with the primary. As a result, angular momentum tends to be accreted in distinct lumps, leading to rapid reorientation of the accreting star over short timescales. The radiative flux is far more focused as bipolar in the case of $\Sigma = 10.0$ g cm^{-1}, consistent with the narrower geometry of the outflow cavity in this case.

Figure 9 shows the azimuthally-averaged radiative flux from the primary protostar as a function of polar angle in each model at times $t = 0.3,\ 0.4,$ and $0.6t_{\rm ff}$. At each of these times, the effect of the presence of protostellar outflow cavities is clearly evident showing polar radiation flux 1.7 to 15 times that at the midplane. The models with protostellar outflow show enhancement of the polar flux relative to the case without outflows by comparable factors. The degree of poleward focusing of the radiation flux diminishes with time due to broadening of the outflow evacuated cavities that focus the radiation. We note that polar flux in the $\Sigma = 1.0$ g cm^{-2} and $\Sigma = 2.0$ g cm^{-2} cases at $t = 0.4t_{\rm ff}$ underrepresents the flux focusing due to outflow cavities because the outflow cavities are tilted by $\sim 20^\circ$ relative to the orientation of the primary protostar shown in figure 8. Similar radiation focusing effects were also shown in Krumholz et al. (2005), where the authors considered the effects of the presence of outflow cavities on radiation escape from the infalling envelope around massive protostars. Using static radiative transfer models they showed that focusing of the radiative force from the central star throughout the outflow cavity results in a reduction of the equatorial radiative flux relative to a control model without outflows by factors of 1.7 to 14, depending on the width and shape of the region of low optical depth in the outflow cavity. Therefore, the models presented here support the Krumholz et al. (2005) prediction that outflows reduce the Eddington radiation pressure barrier to high-mass star formation by reducing the radiation force exerted in the infalling cloud gas. However, it has also been shown that fully 3D Rayleigh-Taylor modes can remove the Eddington barrier even when protostellar outflows are neglected (Krumholz et al. 2009).

3.5. Star Formation Efficiency

Matzner & McKee (2000) give an analytic model for the core to star formation efficiency

$$\epsilon_{\rm core} = 1 - M_{\rm ej}/M, \tag{22}$$

where $M_{\rm ej}$ is the net mass ejected from the core by entrainment into the protostellar outflow and M is the initial core mass. For the case of an unmagnetized core the model predicts

$$\epsilon_{\rm core} = \frac{2X(c_g)}{1 + \sqrt{1 + 4(1+f_w)^2 X^2(c_g)}}, \tag{23}$$

where the dimensionless function X is defined by

$$X = c_g \ln\left(\frac{2}{\theta_0}\right) \frac{v_{\rm esc}}{f_w \bar{v}_w}, \tag{24}$$

$v_{\rm esc}$ is the escape speed from the edge of the core, and the parameter c_g depends on the core density profile and free-fall time relative to the effective timescale for the wind driving. For

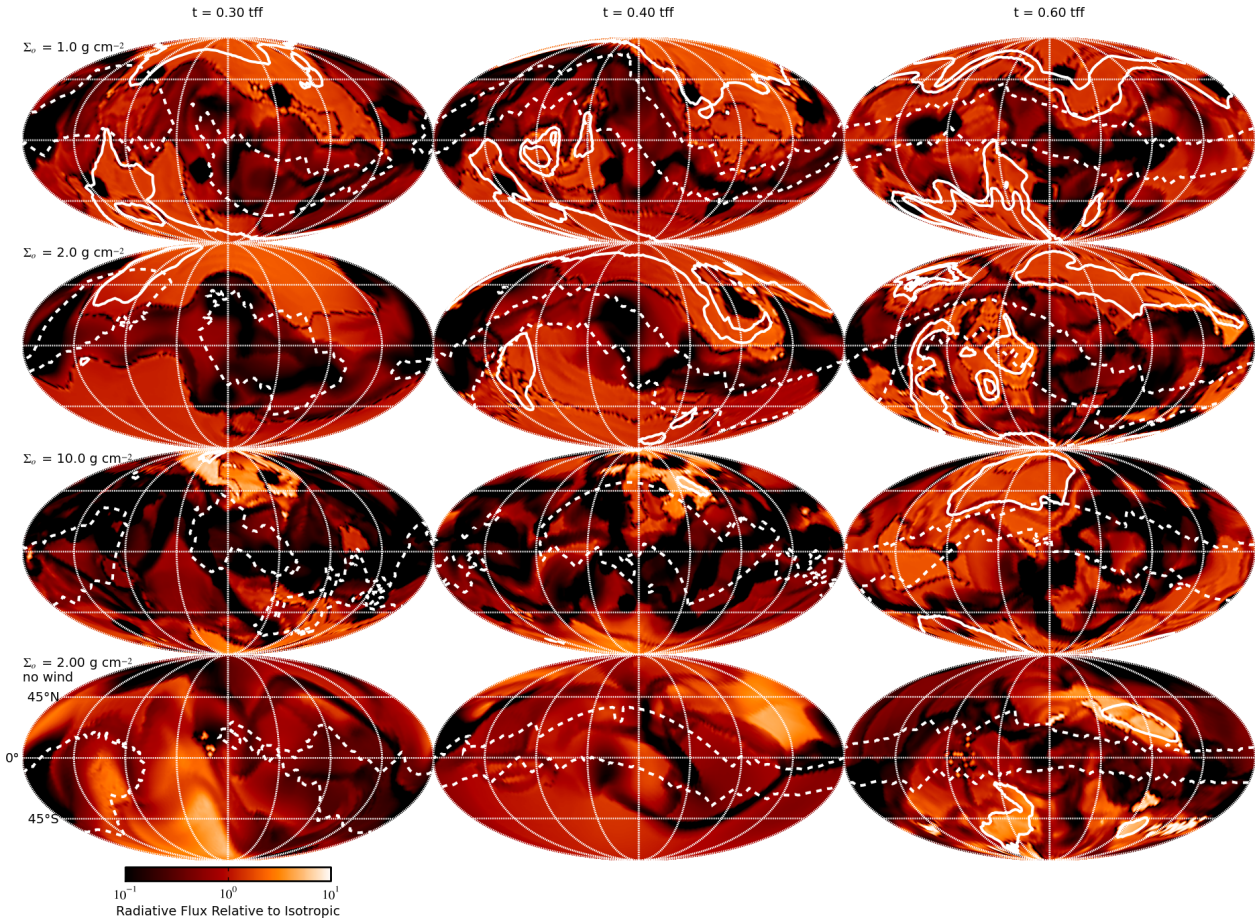

Fig. 8.— Radial component of the radiation flux, normalized to the isotropic flux at 1500 AU from the primary protostar. Columns indicate the times $t = 0.3t_{\rm ff}$, $t = 0.4t_{\rm ff}$ and $t = 0.6t_{\rm ff}$ from left to right and the rows indicate the simulation parameters of $\Sigma = 1.0$ g cm^{-2}, $\Sigma = 2.0$ g cm^{-2}, $\Sigma = 10.0$ g cm^{-2} and $\Sigma = 2.0$ g cm^{-2} without winds from top to bottom. The coordinate system is defined such that the angular momentum of the primary star points northward and the azimuthal coordinate facing the thinnest edge of the cloud due to the motion of the star relative to the center of mass of the system is centered in each of the plots. Contours of the 75$^{\rm th}$ percentile column density from $r = 0$ to 1500 AU are shown as dashed lines and contours of the radial velocities of 20 km s^{-1} and 50 km s^{-1} at $r = 1500$ AU are shown as solid lines.

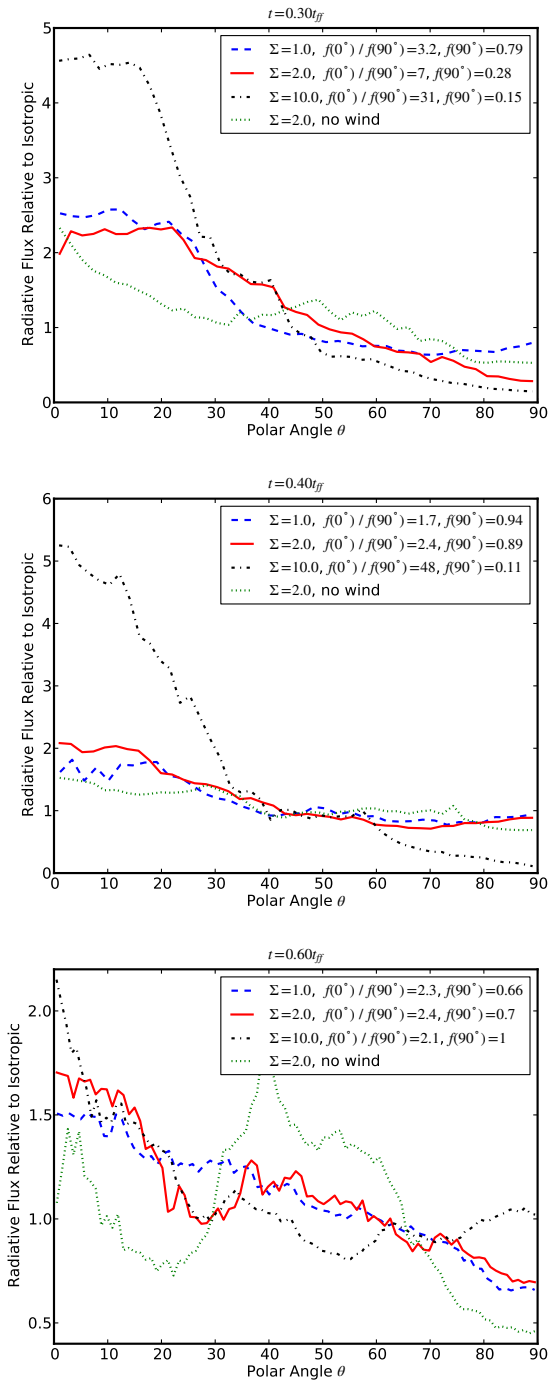

Fig. 9.— Radial component of the radiation flux at 1500 AU in radius from the primary star, normalized to the isotropic flux, as a function of polar angle. The flux shown at a given θ is a volume average over a pair of rings at polar angles $\theta = 0$ and $180° - \theta$ that cover all azimuthal angles ϕ. The coordinate system is oriented so that $\theta = 0$ corresponds to the rotation axis of the primary star and the direction in which the wind is launched.

an unmagnetized core with profile $\rho \propto r^{-3/2}$, equation (A19) of Matzner & McKee (2000) provides an estimate of

$$c_{g,\gg 1} = \frac{\pi(9-3k_\rho)(4-k_\rho)}{8-3k_\rho}\left(\frac{t_w}{t_{\rm ff}}\right) \tag{25}$$

for steady winds. The estimate depends on the the age of the steady wind, t_w and is valid for $c_g \gg 1$. In the limit of an impulsively driven wind, $t_w \to 0$, Matzner & McKee (2000) provide an estimate of

$$c_{g,0} = \sqrt{\frac{9-3k_\rho}{8-3k_\rho}}. \tag{26}$$

To compare our simulations with the analytic model, we choose c_g by interpolating between the two limits as:

$$c_g = \frac{\pi(9-3k_\rho)(4-k_\rho)}{8-3k_\rho}\left(\frac{t_w}{t_{\rm ff}}\right) + \sqrt{\frac{9-3k_\rho}{8-3k_\rho}}. \tag{27}$$

For $k_\rho = 3/2$ this expression becomes

$$c_g = 2.52\frac{t_w}{t_{\rm ff}} + 1.13. \tag{28}$$

The mass-weighted average wind speed that characterizes the wind momentum injection into the core is

$$\bar{v}_w = \sum_{\rm stars} \frac{1}{f_w M_i}\int \dot{M}_{w,i} v_{w,i} dt. \tag{29}$$

Values of $\bar{v}_w$ and $v_{\rm esc}$ are given in table 2. Because our numerical wind injection approach is based on volume-averaged quantities inside of an 8-cell radius wind injection sphere as described in §2.4, the effective numerical flattening parameter is $\theta_{0,\rm eff} = 5.75\times 10^{-4}$ for winds with an opening angle $> 32°$ and we shall use this as the flattening parameter for the purposes of comparing the simulations to the analytic model. We note that X depends logarithmically on the flattening parameter (equation (23)) and therefore the model prediction is not very sensitive to the estimate of the effective numerical flattening angle.

Due to constraints on computational time, we have not run numerical simulations sufficiently long to determine the final star formation efficiency. To facilitate comparison between the numerical and analytic model, we focus our attention to the ratio of the mass ejected by winds to the total stellar mass,

$$\epsilon_{\rm wind} = \frac{M_{\rm ej}}{\sum_{\rm stars} M_i} = \frac{1-\epsilon_{\rm core}}{\epsilon_{\rm core}}, \tag{30}$$

where $M_{\rm ej}$ is the total mass ejected from the system. This quantity can be computed as a function of time throughout the simulation. For the purpose of comparing our numerical

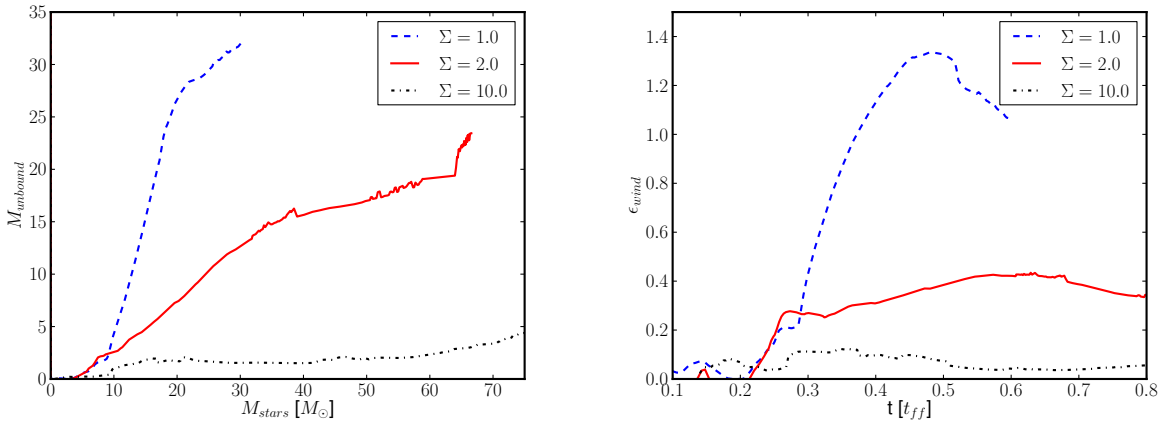

Fig. 10.— Left: Mass with outward radial speed greater than the escape speed of the system as a function of the total mass in stars. Right: Mass with outward radial speed greater than the escape speed relative to the total mass in stars as a function of time.

simulations to the analytic prediction, we heuristically define the ejected mass as any mass that has been either ejected from the simulation domain or that is propagating with a sufficient radial component of velocity away from the center of mass of the system to overcome its gravitational binding to the system. The left panel of figure 10 shows a plot of the total wind mass ejected in each simulation as a function of the total mass in stars and the right panel shows the simulation result for the wind ejection efficiency $\epsilon_{\rm wind} = M_{\rm ej}/\sum_{\rm stars} M_i$ as a function of time for each simulation. We note that wind-launched gas in the highest surface density simulation with $\Sigma = 10.0$ g cm^{-2} emerges from the initial core relatively late in the simulation at $t \sim 0.6t_{\rm ff}$. At the end of the simulation, much of the wind-launched gas is still entrained in the limbs of the outflow cavity. This is a transient effect that is not included in the analytic model and we therefore will focus our attention in comparing the analytic prediction to only the $\Sigma = 1.0$ g cm^{-2} and $\Sigma = 2.0$ g cm^{-2} models. By inspection of figure 10, we adopt the values of $t_w = 0.5t_{\rm ff}$ and $t_w = 0.3t_{\rm ff}$ as characteristic of the age of the winds in the $\Sigma = 1.0$ g cm^{-2} and $\Sigma = 2.0$ g cm^{-2} simulations respectively.

The analytic predictions given by equations (23 & 30) for the outflow mass-weighted wind speed $\bar{v}_w$ for each simulation are given in table 2. The wind ejection efficiency at the end of each simulation ($t = t_{\rm end}$) are listed in the table as $\epsilon_{\rm wind\ simulation}$ for comparison to the model predictions.

In drawing conclusions from comparing the analytic model result for the wind ejection ratio $\epsilon_{\rm wind}$ to the simulation result $\epsilon_{\rm wind\ simulation}$ it is important to bear in mind that the

analytic model predicts the fraction of the initial core that is ejected by a wind over the entire course of evolution of the initial core, whereas the numerical model is only averaged over the duration of the core evolution up to the end of the simulation. Furthermore, the analytic model cannot account for the time dependence associated with the propagation of protostellar wind shocks through the highly inhomogeneous ambient core.

For the lowest surface density case $\Sigma = 1.0$ g cm^{-2}, the simulation has ejected more mass with the wind per unit of mass accretion than predicted by the analytic model by a factor of 2.3. This is likely due to efficient entrainment of core gas into the wind via the interaction of the protostellar winds as they propagate through the network of dense filaments in the ambient core at early time. By $t = 0.4\ t_{\rm ff}$, a wide wind cavity has been cleared through the initial core in the simulation (see the top row of figure 3). The time-integrated outflow ejection behavior in the simulation is biased toward this early-time behavior because the simulations are only advanced to $t = 0.6t_{\rm ff}$ in the $\Sigma = 1.0$ g cm^{-2} case and $t = 0.8t_{\rm ff}$ in the other models. In figure 10, we note that evolution of the system past $0.5t_{\rm ff}$ carries forward with less efficient entrainment of core gas into the outflows as the outflowing gas at later time propagates unimpeded through the wind channel. We expect that with continued evolution the system would asymptote to a steady state value of $\epsilon_{\rm core}$ that is closer to the model prediction. However, constraints of computational cost have prevented us from testing this expectation.

The intermediate surface density case $\Sigma = 2.0$ g cm^{-2} exhibits low ejection efficiency due to during the initial core-crossing of the outflow from $t = 0$ to $t = 0.3t_{\rm ff}$. The ejection efficiency plateaus at later time with $\epsilon_{\rm core}$ varying between 0.34 and 0.42 at later time. We note that by the end of the simulation at $t = 0.8t_{\rm ff}$, the outflow ejection efficiency in the simulation is 92% of the analytic prediction.

Table 2: Outflow ejection simulation results (rows 1-5) and analytic model predictions (rows 6 & 7). The columns indicate the cases of $\Sigma = 1.0$ g cm^{-2}, $\Sigma = 2.0$ g cm^{-2} and $\Sigma = 10.0$ g cm^{-2} from left to right. As discussed in the text, the $\Sigma = 10.0$ g cm^{-2} simulation was not evolved sufficiently far in time to compare with the analytic model.

Σ (g cm^{-2})	1.0	2.0	10.0
$t_{\rm end}$ ($t_{\rm ff}$)	0.6	0.8	0.8
$v_{\rm esc}$ (km s^{-1})	4.27	5.08	7.60
$\bar{v}_w\|_{t=t_{\rm end}}$ (km s^{-1})	87.7	72.2	71.0
$\epsilon_{\rm wind\ simulation}$	1.06	0.342	0.0563
$\epsilon_{\rm core}$	0.70	0.73	–
$\epsilon_{\rm wind}$	0.42	0.370	–

4. Summary

We report the results of several AMR radiation-hydrodynamic simulations of the collapse of massive star forming clouds using the ORION code. These simulations are the first to include the feedback effects of protostellar outflows, radiative heating, and radiation pressure in a single computation. In these simulations, the initial density profile, velocity spectrum, virial ratio and numerical resolution are held constant. The simulations are scaled to different surface density to study the environmental dependence of the outflow and radiation feedback, and in one case the surface density is held constant but outflow feedback is turned off to isolate the effect of protostellar outflow.

Comparison of models with protostellar outflow feedback and surface densities $\Sigma = 1.0$ g cm^{-2}, $\Sigma = 2.0$ g cm^{-2} and $\Sigma = 10.0$ g cm^{-2} at equivalent free-fall time shows that the higher surface density clouds exhibit enhanced radiative heating feedback, diminished disk fragmentation and host more massive primary stars with less massive companions. However, the effects of outflow feedback diminish with increased surface density. Lower surface density clouds have longer free-fall time and therefore undergo more Kelvin contraction in the primary protostellar core, leading to more powerful outflows and more effective mechanical feedback. Furthermore, lower surface density clouds give rise to protostellar outflows with shorter core crossing time relative to the core free-fall time and these clouds are consequently influenced by the effect of outflows at relatively earlier stages of collapse.

Comparison of models with and without outflow feedback at surface density $\Sigma = 2.0$ g cm^{-2} indicates a strong coupling between outflow and radiative feedback on the parent cloud. Outflow activity produces polar cavity of reduced optical depth through the ambient core. Radiation focusing in the direction of outflow cavities is sufficient to prevent the formation of radiation pressure-supported circumstellar gas bubbles, in contrast to models which neglect protostellar outflow feedback. With outflows, the radiative flux in the poleward direction is enhanced by 1.7 to 15 times that in the midplane. Sheets with outward radiative flux reduction up to an order of magnitude appear near the equatorial latitude of the primary star in all of the models with protostellar outflow. This result is consistent with the predictions of Krumholz et al. (2005) that focusing of the radiative flux from the central star throughout the outflow cavity results in a reduction of the equatorial radiative flux relative to a control model without outflows by factors of 1.7 to 14, depending on the geometry of the outflow cavity. As a result the radiative heating and outward radiation force exerted on the protostellar disk and infalling cloud gas in the equatorial direction is greatly diminished by the presence of the outflow cavity, and our models support the Krumholz et al. (2005) prediction that outflows reduce the Eddington radiation pressure barrier to high-mass star formation by reducing the radiation force exerted in the infalling cloud gas.

Precisely determining the effect of outflows on the threshold density prediction for massive star formation will require examination of simulations at lower cloud surface density than the models presented here. Furthermore, we expect that the relative importance of this effect may depend on the role of magnetic fields in confining the outflow cavity. Future works should therefore examine the effect of protostellar outflows in lower surface density, magnetized clouds.

Support for this work was provided by: the US Department of Energy at the Lawrence Livermore National Laboratory under contract DE-AC52-07NA 27344 (AJC and RIK); an Alfred P. Sloan Fellowship (MRK); NASA through ATFP grant NNX09AK31G (RIK, CFM, and MRK); NASA as a part of the Spitzer Theoretical Research Program, through a contract issued by the JPL (MRK and CFM); the National Science Foundation through grants AST-0807739 (MRK) and AST-0908553 (RIK and CFM). Support for computer simulations was provided by an LRAC grant from the National Science Foundation through TeraGrid resouces, the Arctic Region Supercomputing Center (ARSC) and the NASA Advanced Supercomputing Division. The YT software toolkit (Turk et al. 2011) was used for the data analysis and plotting.

REFERENCES

Arce, H. G., Borkin, M. A., Goodman, A. A., Pineda, J. E., & Halle, M. W. 2010, ApJ, 715, 1170

Arce, H. G., & Sargent, A. I. 2006, ApJ, 646, 1070

Bachiller, R. 1996, ARA&A, 34, 111

Bertoldi, F., & McKee, C. F. 1992, ApJ, 395, 140

Beuther, H., Leurini, S., Schilke, P., Wyrowski, F., Menten, K. M., & Zhang, Q. 2007, A&A, 466, 1065

Beuther, H., Schilke, P., & Gueth, F. 2004, ApJ, 608, 330

Beuther, H., Schilke, P., Gueth, F., McCaughrean, M., Andersen, M., Sridharan, T. K., & Menten, K. M. 2002, A&A, 387, 931

Beuther, H., Schilke, P., Menten, K. M., Motte, F., Sridharan, T. K., & Wyrowski, F. 2002, ApJ, 566, 945

Beuther, H., Schilke, P., & Stanke, T. 2003, A&A, 408, 601

Beuther, H., Walsh, A., Schilke, P., Sridharan, T. K., Menten, K. M., & Wyrowski, F. 2002, A&A, 390, 289

Beuther, H., & Shepherd, D. 2005, Cores to Clusters: Star Formation with Next Generation Telescopes, 105

Carrasco-González, C., Rodríguez, L. F., Anglada, G., Martí, J., Torrelles, J. M., & Osorio, M. 2010, Science, 330, 1209

Carroll, J. J., Frank, A., & Blackman, E. G. 2010, ApJ, 722, 145

Chandler, C. J., & Richer, J. S. 2000, ApJ, 530, 851

Crowther, P. A., Schnurr, O., Hirschi, R., Yusof, N., Parker, R. J., Goodwin, S. P., & Kassim, H. A. 2010, MNRAS, 408, 731

Cunningham, A. J., Frank, A., & Blackman, E. G. 2006, ApJ, 646, 1059

Curiel, S., et al. 2006, ApJ, 638, 878

Egan, M. P., Shipman, R. F., Price, S. D., Carey, S. J., Clark, F. O., & Cohen, M. 1998, ApJ, 494, L199

Goodman, A. A., Benson, P. J., Fuller, G. A., & Myers, P. C. 1993, ApJ, 406, 528

Hennebelle, P., Commercon, B., Joos, M., Klessen, R. S., Krumholz, M., Tan, J. C., & Teyssier, R. 2011, arXiv:1101.1574

Hutawarakorn, B., Cohen, R. J., & Brebner, G. C. 2002, MNRAS, 330, 349

Jacquet, E., & Krumholz, M. 2011, arXiv:1101.5265

Jijina, J., & Adams, F. C. 1996, ApJ, 462, 874

Klein, R. I. 1999, Journal of Computational and Applied Mathematics, 109, 123

Krumholz, M. R., Cunningham, A. J., Klein, R. I., & McKee, C. F. 2010, ApJ, 713, 1120

Krumholz, M. R., Klein, R. I., & McKee, C. F. 2007, ApJ, 656, 959

Krumholz, M. R., Klein, R. I., McKee, C. F., & Bolstad, J. 2007, ApJ, 667, 626

Krumholz, M. R., Klein, R. I., McKee, C. F., Offner, S. S. R., & Cunningham, A. J. 2009, Science, 323, 754

Krumholz, M. R., & McKee, C. F. 2008, Nature, 451, 1082

Krumholz, M. R., McKee, C. F., & Klein, R. I. 2005, ApJ, 618, L33

Krumholz, M. R., McKee, C. F., & Klein, R. I. 2004, ApJ, 611, 399

Kuiper, R., Klahr, H., Beuther, H., & Henning, T. 2010, ApJ, 722, 1556

Lada, C. J. 2006, ApJ, 640, L63

Larson, R. B., & Starrfield, S. 1971, A&A, 13, 190

López-Sepulcre, A., Cesaroni, R., & Walmsley, C. M. 2010, A&A, 517, A66

López-Sepulcre, A., et al. 2011, A&A, 526, L2

Matzner, C. D., & McKee, C. F. 1999, ApJ, 526, L109

Matzner, C. D., & McKee, C. F. 2000, ApJ, 545, 364

McCrady, N., & Graham, J. R. 2007, ApJ, 663, 844

McKee, C. F. 1989, ApJ, 345, 782

McKee, C. F., & Ostriker, E. C. 2007, ARA&A, 45, 565

McKee, C. F., & Tan, J. C. 2002, Nature, 416, 59

McKee, C. F., & Tan, J. C. 2003, ApJ, 585, 850

Myers, A. T., Krumholz, M. R., Klein, R. I., McKee, C. F., & Tan, J. C. 2011, in prep.

Nakamura, F., & Li, Z.-Y. 2007, ApJ, 662, 395

Nakano, T. 1989, ApJ, 345, 464

Norman, C., & Silk, J. 1980, ApJ, 238, 158

Nürnberger, D. E. A., Chini, R., Eisenhauer, F., Kissler-Patig, M., Modigliani, A., Siebenmorgen, R., Sterzik, M. F., & Szeifert, T. 2007, A&A, 465, 931

Offner, S. S. R., Klein, R. I., McKee, C. F., & Krumholz, M. R. 2009, ApJ, 703, 131

Patel, N. A., et al. 2005, Nature, 437, 109

Pelletier, G., & Pudritz, R. E. 1992, ApJ, 394, 117

Peters, T., Klessen, R. S., Mac Low, M.-M., & Banerjee, R. 2010, ApJ, 725, 134

Perault, M., et al. 1996, A&A, 315, L165

Preibisch, T., Weigelt, G., & Zinnecker, H. 2001, The Formation of Binary Stars, 200, 69

Qiu, K., Zhang, Q., Beuther, H., & Yang, J. 2007, ApJ, 654, 361

Radhakrishnan, K. & Hindmarsh, A. C. 1993, LLNL report UCRL-ID-113855.

Rathborne, J. M., Jackson, J. M., & Simon, R. 2006, ApJ, 641, 389

Rathborne, J. M., Simon, R., & Jackson, J. M. 2007, ApJ, 662, 1082

Richer, J. S., Shepherd, D. S., Cabrit, S., Bachiller, R., & Churchwell, E. 2000, Protostars and Planets IV, 867

Rodriguez, L. F. 1997, Herbig-Haro Flows and the Birth of Stars, 182, 83

Saraceno, P., Andre, P., Ceccarelli, C., Griffin, M., & Molinari, S. 1996, A&A, 309, 827

Semenov, D., Henning, T., Helling, C., Ilgner, M., & Sedlmayr, E. 2003, A&A, 410, 611

Shatsky, N., & Tokovinin, A. 2002, A&A, 382, 92

Shepherd, D. 2003, Galactic Star Formation Across the Stellar Mass Spectrum, 287, 333

Shepherd, D. S., & Churchwell, E. 1996, ApJ, 472, 225

Shu, F. H., Adams, F. C., & Lizano, S. 1987, ARA&A, 25, 23

Shu, F. H., Lizano, S., Ruden, S. P., & Najita, J. 1988, ApJ, 328, L19

Swift, J. J. 2009, ApJ, 705, 1456

Toomre, A. 1964, ApJ, 139, 1217

Torrelles, J. M., Gomez, J. F., Rodriguez, L. F., Ho, P. T. P., Curiel, S., & Vazquez, R. 1997, ApJ, 489, 744

Truelove, J. K. 1997, Ph.D. Thesis

Truelove, J. K., Klein, R. I., McKee, C. F., Holliman, J. H., II, Howell, L. H., & Greenough, J. A. 1997, ApJ, 489, L179

Truelove, J. K., Klein, R. I., McKee, C. F., Holliman, J. H., II, Howell, L. H., Greenough, J. A., & Woods, D. T. 1998, ApJ, 495, 821

Turk, M. J., Smith, B. D., Oishi, J. S., Skory, S., Skillman, S. W., Abel, T., & Norman, M. L. 2011, ApJS, 192, 9

Turner, J. L., Beck, S. C., & Ho, P. T. P. 2000, ApJ, 532, L109

Walawender, J., Bally, J., & Reipurth, B. 2005, AJ, 129, 2308

Wang, P., Li, Z.-Y., Abel, T., & Nakamura, F. 2010, ApJ, 709, 27

Yorke, H. W., & Sonnhalter, C. 2002, ApJ, 569, 846

Zhang, Q., Hunter, T. R., Brand, J., Sridharan, T. K., Molinari, S., Kramer, M. A., & Cesaroni, R. 2001, ApJ, 552, L167

Zinnecker, H., & Yorke, H. W. 2007, ARA&A, 45, 481